Journal of
Materials Chemistry A
Materials for energy and sustainability

This article can be cited before page numbers have been issued, to do this please use: L. G. Gong, X. Qi, K. Yu, J. Gao, B. Zhou and G. Yang, *J. Mater. Chem. A*, 2020, DOI: 10.1039/C9TA14103K.

ROYAL SOCIETY
OF CHEMISTRY

rsc.li/materials-a

View Article Online
DOI: 10.1039/C9TA14103K

Journal Name

ARTICLE

Received 00th January 20xx,
Accepted 00th January 20xx

DOI: 10.1039/x0xx00000x

www.rsc.org/

Covalent conductive polymer chain and organic ligand ethylenediamine modified MXene-like-$\{AlW_{12}O_{40}\}$ compounds for fully symmetric supercapacitors, electrochemical sensors and photocatalysis mechanisms

Li-Ge Gong[a], Xian-Xian Qi[a], Kai Yu[a*], Jia-Qian Gao[a], Bai-Bin Zhou[a*], Guo-Yu Yang[b*]

We successfully synthesized two kinetically stable the covalent polymer chains and ethylenediamine acting MXene-like-$\{AlW_{12}O_{40}\}$ compounds. According to the results of energy storage research, these materials show high capacitance performance and cycle stability. The capacitors of **1**-CC(carbon cloth) and **2**-CC are 478.41 and 625.99F g^{-1}(1.0 A g^{-1}), and the capacitance retention is 95.71% and 97.62% after 5000 cycles. The symmetrical water system supercapacitor device is assembled with two **2**-CC and the energy density of 6.32Wh kg^{-1} at 237W kg^{-1}. Meanwhile, compounds **1-2** were used to test the new sensitive current hydrogen peroxide sensor, display that the linear ranges are 1.20-3.20mM(**1**-GCE:glassy carbon electrode) and 19.95μM-0.90mM(**2**-GCE) with the detection limit of 0.93μM, 0.86μM. In addition, the photocatalysis mechanisms of compounds **1-2** were studied to provide a powerful basis for the photocatalytic mechanism of this series of compounds.

Introduction

With the rapid growth of the world's population, the deterioration of the ecological environment and the shortage of fossil resources left people urgently to pursue sustainable and renewable energy, which in turn promotes the vigorous development of various clean, efficient energy conversion and storage equipment, such as, lithium-ion batteries[1-6] supercapacitors (SCs)[7-15] and fuel cells[16-20]. Among them, SCs have emerged from the numerous energy storage devices because of their fast charging ability, long cycles stability, high power density and environmental friendliness[21-22]. However, electrode materials are one of the important factors that affect the capacitance of SCs. The research on electrode materials which improve the specific capacitance and cycles stability has grown up to be a hot topic in the research of high performance SCs.

Polyoxometalates (POMs), an outstanding class of metal-oxygen clusters, possess unparalleled versatile physical and chemical properties, including attractive well-defined structures, regular sizes, superior redox properties and can be used as electron reservoirs[23-26]. In view of the generality mentioned above, POMs can be exploited in many fields, such as electrochemistry[27], energy storage/conversion[28], magnetism[29], catalysis[30-31], photochemistry[32], ionic conductors[33], medicine[34-39] and sensors[40-45]. In particular, POMs have discrete ionic structures, including heteropoly anions and movable countercations, such as H^+, H_3O^+. This unique structural feature enables POMs to perform fast and reversible stepwise numerous electrons transfer reactions without changing their structures, which makes POMs an excellent candidate for supercapacitor electrode materials. However, POMs have some shortcomings, such as the high solubility, poor cycling ability and conductivity. To overcome these problems, many researchers have proposed some solutions. On the one hand, since Gomez-Romero et al.[46] first reported that hybrid nanocomposites formed by Polyaniline and $H_3PMO_{12}O_{40}$ as electrodes for supercapacitor, there have been some reports[47-48] of composites based on POMs and conductive polymers materials. Conductive polymers can improve the conductivity of POMs and facilitate electron transfer. However, immobilization of POMs into a polymer matrix limits the redox active sites of POMs and thus constrains their supercapacitor performance.[49] On the other hand, some researchers[50-53] have proposed the synthesis of hybrid coordination polymers by covalent bonding of transition metals, organic ligands and POMs to solve the problem of high solubility and low conductivity,but the low cycle stability has not been alleviated.

Therefore, we propose a new approach based on the above-mentioned researchers' approach: (1) Among central atoms of the most Keggin type POMs are mainly group 14 and 15 elements and some transition metals, which group 13 as central atoms have been rarely extensively exploration[54-55]. It is noted that aluminium atoms

---

[a] Key Laboratory for Photonic and Electronic Band gap Materials, Ministry of Education, Harbin Normal University, Harbin 150025, People's Republic of China.E-mail: hlyukai188@163.com, zhou_bai_bin@163.com

[b] MOE Key Laboratory of Cluster Science, School of Chemistry, Beijing Institute of Technology,Beijing, 100081 (China).Email:ygy@bit.edu.cn

View Article Online
DOI: 10.1039/C9TA14404K

can not only as coordination atom[56-59], but also be used as the central atom, which the introducing of Al^{3+} into the center of Keggin structure makes it easier to coordinate to transition metals and gives a wider kind of coordination types, owing to the $[AlW_{12}O_{40}]^{5-}$ anion possesses higher surface charge density[60]. At the same time, the aluminum atom is a boron group element which is electron-deficient and has a strong tendency to make full use of valence orbitals in order to enhance the stability of the system[61]. (2) $[AlW_{12}O_{40}]^{5-}$ anion connects with the chain of transition metal complexes similar to conductive polymers through covalent bonds, which not only solves the problems of high solubility and poor circulation, but also increases the conductive energy and specific capacitance of the composites. As d^{10} transition-metal, the Ag(I) and Cu(I) possesses high affinity for O and N donors,various coordination numbers and versatile geometries[62-69]. 4, 4-bipyridine is an organic ligands similar to pyrrole, which contains many N donors to facilitate coordination with metal ions. These features make Ag(I) and Cu(I) to use as a metallic linker to construct transition metal complexes with 4,4-bipyridine ligands. (3) The small ligand ethylenediamine was introduced to increase the interaction between POMs and transition metal complexes to reduce the resistance of the whole compound.

In this work, we prepared two new organic-inorganic hybrid compounds, $[Ag(bpy)][\{Ag(Hbpy)\}_2(AlW_{12}O_{40})]\cdot H_2O$ (1), $[H_2en][\{Cu(bpy)\}_3(AlW_{12}O_{40})]\cdot 3H_2O$ (2). The compounds **1-2** as electrode materials have high capacitance and excellent cycling ability and have been assembled into symmetrical SCs. In addition, the electrochemical sensors and photocatalytic mechanisms of compounds **1-2** were studied in detail.

Results and discussion

Crystal structure

The structures of compounds **1** and **2** are all built on $[\alpha\text{-}AlW_{12}O_{40}]^{5-}$ (abbreviated as $\{AlW_{12}\}$) and the transition metal complexes. The $\{AlW_{12}\}$ consists of a central AlO_4 tetrahedron surrounded by four vertex-sharing W_3O_{13} groups. Each W_3O_{13} group is composed of three WO_6 octahedra linked in a triangular arrangement by sharing edges, and these four W_3O_{13} groups are linked together by sharing corners. The central Al-O distances vary from 1.72(7)-1.75(8)Å in **1** and 1.74(9)-1.76(11)Å in **2**, respectively. All bond distances are equal to the reported range. $\{AlW_{12}\}$ possesses four kinds of oxygen atoms, the terminal oxygen atoms(O_t), edge-sharing bridging oxygen atoms(O_b), corner-sharing bridging oxygen atoms(O_c), and central oxygen atoms(O_a). Therefore, for compounds **1-2**, W-O distances are 1.64(3)-2.41(4) Å and 1.69(6)-2.28(5) Å, respectively.

Crystal structure analysis reveals that compound **1** consists of $\{AlW_{12}\}$, $[\{Ag(Hbpy)\}_2]^{4+}$ and $[Ag(bpy)]^+$. As shown in Fig.S1, there is two crystallographically independent Ag ions(Ag1, Ag2) in **1**: Ag1 ion exhibits a linear geometry coordinated by two nitrogen atoms from two 4,4'-bipy ligands [Ag-N:2.10(3)]. Each Ag1 ion links 4,4'-bipy ligands into a one-dimensional polymeric chain [namely,$\{$-4,4'-bipy-Ag1-4,4'-bipy-Ag1-$\}_n$]. Ag2 ion adopts T-shaped geometry, which links with two N atoms from two 4,4'-bipy ligands [Ag-N:2.11(3)-2.14(3)Å] and one $\{AlW_{12}\}$ [Ag-O:2.64(3)Å]. each Ag2 ion links 4,4'-bipy ligands into a one-dimensional polymeric chain [namely, $\{$-4,4'-bipy-Ag2-4,4'-bipy-$\}_n$.

In the structure, each Ag2 ions from two $\{$-4,4'-bipy-Ag2-4,4'-bipy-$\}_n$ chains link $\{AlW_{12}\}$ units through O_t atoms to form a 1D ladder chain(Fig.S2). The most intriguing feature of **1** is the novel 2D sheet structure(Fig.S3a) constructed by the strong polymerization between that of the adjacent 1D ladder chain and $\{AlW_{12}\}$ polyoxoanion. In this 2D structure, the $\{$-4,4'-bipy-Ag1-4,4'-bipy-Ag1-$\}_n$ chains are linked not only to $[AlW_{12}O_{40}]^{5-}$ units through supramolecular interaction, but also to $\{$-4,4'-bipy-Ag2-4,4'-bipy-$\}_n$ through π-π stacking interaction to form a new 2,4,6-connected topology structure(Fig.S3b) with the aperture of 19.12×16.28 $Å^2$. In this topology structure, Ag1 ions were assigned as four-connected nodes, Ag2 ions as two-connected nodes and $\{AlW_{12}\}$ as six-connected nodes, then the topology symbol is $\{4.6^4.8\}\{4^6.6.8^4.10^4\}\{4\}_2$. Besides, 2D layers formed 3D network via π-π stacking interactions of $\{$-4,4'-bipy-Ag1-4,4'-bipy-Ag1-$\}_n$ chains of adjacent layers(Fig. S4).

In the overall structure of compound 1, $\{$-4,4'-bipy-Ag1-4,4'-bipy-Ag1-$\}_n$ polymer chain form a 1D pipe structure(Fig.1a) by connecting oxygen from $\{AlW_{12}\}$(Fig.1b), and$\{$-4,4'-bipy-Ag2-4,4'-bipy-$\}_n$ polymer chain(Fig.1c) is located in the 1D pipe through hydrogen bonding and supramolecular interaction. The 1D pipe connected with $\{AlW_{12}\}$ to form a MXene-like layer structure[70-71]. Each MXene-like layer forms a 3D stacking structure(Fig.1d-e) through hydrogen bonding and supramolecular interaction, and the distance between the layers is 11.36Å. The structure similar to MXene with metal polymer chains is beneficial to increase the migration speed and conductivity of ions and electron for SCs.

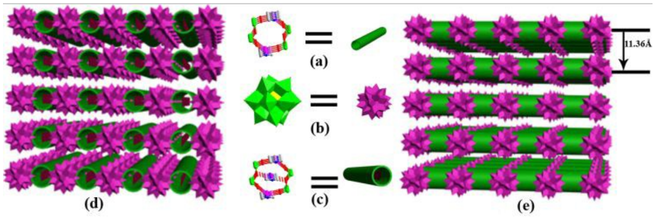

Fig 1. The 3D structure of compound **1**: (a) 1D pipe structure (b) $\{AlW_{12}\}$ (c)$\{$-4,4'-bipy-Ag2-4,4'-bipy-$\}_n$ polymer chain is located in the 1D pipe (d) The front view (e)The side view

Crystal structure analysis reveals that compound **2** consists of one $\{AlW_{12}\}$, three $[Cu(4,4'\text{-}bipy)]^+$ fragments and $[H_2en]^{2+}$. As shown in Fig.S5, there are three crystallographically independent Cu ions in **2**: Cu1, Cu2 and Cu3 ions adopt T-shaped geometry, which link with two N atoms from two 4,4'-bipy ligands and one $\{AlW_{12}\}$ polyoxoanion through a bridging oxygen atom(for Cu3) or a terminal oxygen atom (for Cu1 and Cu2). The bond lengths of Cu-N are in the range of 1.89(7)-1.91(8)Å and Cu-O is 2.32(6)Å. Moreover, Cu1,Cu2 and Cu3 formed two p olymer chains with 4,4'-bipy ligands, (namely, $\{$-4,4'-bipy-Cu1-4,4'-bipy-Cu3-$\}_n$ and $\{$-4,4'-bipy-Cu2-4,4'-bipy-Cu2-$\}_n$). $\{$-4,4'-bipy-Cu1-4,4'-bipy-Cu3-$\}_n$ and $\{$-

4,4’-bipy-Cu2-4,4’-bipy-Cu2-}$_n$) are parallel to each other to form an ABAB polymer plane.

In the structure of compound **2**, $\{AlW_{12}\}$ units link Cu3 ions from two {-4,4’-bipy-Cu2-4,4’-bipy-}$_n$ chains through terminal oxygen atoms to form a 1D chain(Fig.S6). The adjacent 1D ladder chains are connected by two {-4,4’-bipy- Cu1-4,4’-bipy-Cu3-}$_n$ chains and {-4,4’-bipy-Cu2-4,4’-bipy-Cu2-}$_n$ chain form a fascinating sheet structure(Fig.S7a) with a new topology. In this topology structure(Fig.S7b), Cu1 ions were assigned as three-connected nodes, Cu2 ions as three-connected nodes, Cu3 ions as four-connected nodes and $\{AlW_{12}\}$ polyoxoanion as four-connected nodes, then the topology symbol is $\{6^2.8\}\{6^4.8^2\}$ with the different sizes of holes (ABAB arrange), 19.41×15.36Å² and 17.90×17.10Å², respectively. Furthermore, 2D layer interacts with ethylenediamine molecules through hydrogen bond to form 3D network (see Fig. S8).

From the whole structure, compound **2** is more characteristic than compound **1**. On the one hand, compound **2** has a 1D ions pipeline(Fig. 2a) formed by the connection between the same polymer chain with {-4,4’-bipy-Cu1-4,4’-bipy-Cu3-}$_n$ and the terminal oxygen from $\{AlW_{12}\}$(Fig. 2b), and {-4,4’-bipy-Cu2-4,4’-bipy-Cu2-}$_n$ is occupied in the 1D pipe through the covalent bond intereaction. On the other hand, the addition of ethylenediamine(Fig. 2c) increases the interaction between the a MXene-like layers to form a 3D structure (Fig. 2d-e)with the wider layer spacing of 13.71 Å, which makes compound **2** had better ion and electron transport ability than compound **1**.

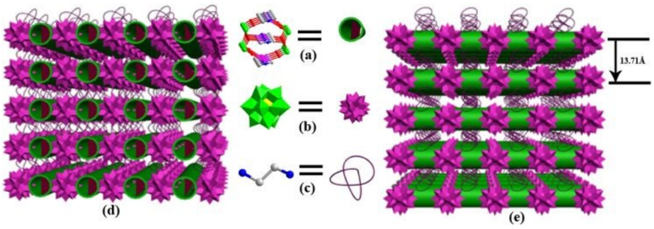

Fig 2. The 3D structure of compound **2**: (a) $\{AlW_{12}\}$ (b){-4,4’[-bipy-Cu2-4,4’-bipy-Cu2-}$_n$ is occupied in the 1D pipe (c) ethylenediamine (d) The front view (e) The side view

Structural and morphology characteristics of compounds 1-2

The valence bond calculation(BVS)[72] shows that the average values of the W centers of compounds **1** and **2** are 5.87 and 5.92, respectively, which are equal to almost all W atoms in the +6 oxidation state. At the same time, BVS calculation shows that all Ag and Cu centers are in the oxidation state of +1 for compounds **1-2**. In addition, one extra proton is added to the bipyridine ligand in compound **1** and two extra protons should be added to the ethylenediamine ligand in compound **2** to achieve charge balance, which is consistent with the acid reaction environment.

The IR spectra of compounds are shown in Fig.S9, which exhibits characteristic vibration patterns derived from the Keggin polyoxoanions in 700-1000 cm^{-1}. There are four characteristic bands in the IR spectra appearing at 953, 887, 802, and 766cm^{-1} for **1**, and 962, 882, 812, and 761 cm^{-1} for **2**, respectively, which can be assigned to v(W-O_t), v(Al-O_a), v(W-O_b), and v(W-O_c)[73]. In addition, the characteristic absorption bands in the range of 1208-1612cm^{-1} for compounds **1** and **2** are attributed to the en and 4,4’-bipy ligands. The peaks at 3496 and 3442cm^{-1} are assigned to the vibration of water molecules for compounds **1** and **2**.

View Article Online
DOI: 10.1039/C9TA14103K

To investigate the thermal stabilities of compounds **1** and **2**, TG analyses were carried out, as shown in Fig.S10. From the TG curves, the weight loss processes both have two weight loss steps. In compound **1** (Fig.S10a), the first weight loss of 0.55% between 50-265 ℃ could be attributed to the loss of water molecules(calc. 0.48%). The second weight loss of 12.72% in the range of 500-700℃ assigned to the loss of 4,4’-bipy molecules (calc.12.60%). In Fig.S10b, the TG curve for **2** shows a first weight loss of 0.74% between 30-200 ℃ suggesting the loss of water molecules (calcd.1.48%). When the temperatures increases from 500 to 750℃, the weight loses 13.00% indicating the loss of 4,4’-bipy and en molecules (calcd. 14.54%).The weight losses from the TG curves are consistent with the molecular formula of compound **1** and **2**. The XRD patterns for compounds **1** and **2** are presented in the Fig. S11. The diffraction peaks of both simulated and experimental patterns are matched, thus indicating that the phase purity of the compounds **1** and **2** are good. The differences of intensity may be due to the preferred orientation of the crystal samples.The UV spectra are measured in the solid state as shown in Fig.S12 in the range of 200-800nm. Two absorption bands appear at 215-217 nm and 290-320 nm for **1-2** in the UV spectras, which are attributed to pπ(Oterminal)→dπ*(M) electronic transitions in the W=O bonds and dπ-pπ-dπ electronic transitions between the energetic levels of the W-O-W bonds[74], respectively.

The surveys of diffuse reflectivity for powder samples of **1-2** were used to gain their band gaps (*E*g), which were determined as the intersection point between the energy axis and the line extrapolated from the linear portion of the adsorption edge in a plot of Kubelka-Munk (K-M) function (*F*) versus energy (*E*). As shown in Fig.S13, the Eg values assessed from the steep absorption edge of **1** and **2** were 2.90eV for **1** and 2.95eV for **2**. The reflectance spectra suggested that compounds **1-2** would be potential photocatalysts, because of the presence of an optical band gap and the semiconducting properties.

The Barrett-Emmett-Teller (BET) specific surface area of the samples are measured by the t-plot method. The values of the BET surface area and langmuir surface area are 65.73 and 115.49 m^2/g for compound 1, 87.74 and 158.25 m^2/g for compound 2(Fig S14). The average desorption pore sizes(Fig. S15) from DFT method are 3.41nm for compound **1** and 2.13 nm for compound **2**. As shown in Fig.S16a-b, the XPS of the compound **1**(or compound **2**) has Ag(or Cu), W, O, Al, N and C elements, and the slight difference between the atomic ratio and the molecular formula is due to the fact that the XPS test does not contain H atoms. Two peaks[75] at 37.68, 35.48eV for compound **1** and 37.33, 35.13eV for compound **2** may attribute to the $W4f_{7/2}$ and $W4f_{5/2}$ core levels of W^{6+}, respectively (Fig. S17a and Fig. S18a). The Al_{2p} spectrum has a main peaks of 73.17eV for compound **1** and 73.30eV for compound **2**,

View Article Online
DOI: 10.1039/C9TA14103K

respectively(Fig. S17b and Fig. S18b), showing that the existence of Al^{3+}. The C spectra has a main peaks of 284.9eV for compound **1** and 284.59eV for compound **2**, respectively(Fig. S17c and Fig. S18c), which belongs to the C_{1s}. The N_{1s} spectrum[48] is divided into two peaks(Fig. S17d and Fig. S18d), which can be attributed to the -N= and-NH^+-/-NH-fragments (399.38 and 401.68eV for compound **1** and 399.2 and 401.6eV for compound **2**). The O_{1s} spectra reveal the co-existence of C-O and C=O (532.08 and 531eV for compound **1** and 532.1 and 531eV for compound **2**). Furthermore, the Ag_{3d} spectrum has two main peaks of 368.08 and 374.08eV for compound **1**, and they can clearly demonstrate the existence of Ag^+ (Figure S17e). In addition, the Cu_{2p} spectrum has a main peak at the 932.9eV, and the existence of Cu^+ (Fig. S18e) for compound **2**.

As shown in Fig.S19a, S21a, the SEM of compounds **1** and **2** show the morphology of block shape and the length and width of 400μm × 297μm for compound **1** and 314μm × 107μm for compound **2**, respectively. EDS microanalysis of compounds **1** and **2** were shown in Fig.S19b, S21b, which can be clearly seen in that the elements O, C, Al, Cu(or Ag), N, and W were existenced. At the same time, mapping diagram(Fig.S20 and S22) further confirmed that the composition of compounds **1-2** were equably distributed.

Electrochemical measurements

Cyclic voltammetry studies

The unique polymer chains, the small molecule ligands of ethylenediamine, and multi-electron transfer process of **$Na_5AlW_{12}O_{40}$-, 1-** and **2**-CC provoke us to further investigate their potential applications in SCs. Three-electrode cyclic voltammetry (CV) curves at the 20 mV s^{-1} scan rate in 0.5M H_2SO_4 are presented in Fig. 3a. The specific capacitances of these compounds are correlated to the average areas of the CV curves which follow the order of **2**-CC> **1**-CC> **$Na_5AlW_{12}O_{40}$**-CC. With the same $\{AlW_{12}\}$ polyanions, the specific capacitances of **2**-CC with {-4,4'-bipy-Cu-4,4' -bipy}$_n$ polymer chains and small-molecule ethylenediamine ligands are much higher than **1**-CC with {-4,4'-bipy-Ag-4,4'-bipy}$_n$, and the capacitance of the $Na_5AlW_{12}O_{40}$ is the smallest of the three compounds. These results clearly demonstrate that the specific capacitances of $\{AlW_{12}\}$ materials are related to the polymer chains and small-molecule ligands as well as their structural features. Fig. S23 and Fig. 3b show the CV curves of **1**-CC and **2**-CC with a potential window from -0.2 to 0.9 V at different scanning rates. Clearly, **1**-CC and **2**-CC show the quadrilateral shape with a pair of redox peaks, indicating the coexistence of both the electrical double-layer capacitance and pseudocapacitance. With the increase of scan rates, the current response is likewise gradually increased, exhibiting good capacitive behaviour and charge storage characteristics.

To further analyze the total charge storage (capacitive and diffusion controlled charge contributions) of **$Na_5AlW_{12}O_{40}$-**, **1-** and **2**-CC electrodes were achieved by estimating the current response of CV curves. It is known that the peak current usually follows the power law relationship with the scan rates. As showed in equation (1):

$$\mathbf{i = av^b} \qquad (1)$$

where a and b are the coefficients, *i* is the peak current density(A), and *v* is the scan rate (mV s^{-1}). The calculated value of b can be distributed into capacitive and diffusion controlled charge contributions for the charge storage mechanism in the electrode material. If b=0.5 ($i \propto v^{1/2}$) for the diffusion-controlled charges (Q_d) and b=1 ($i \propto v$) for the surface capacitive (Q_s). As shown in Fig. S24 and Fig.3c, a good linear relationship is observed between log(current density) and log(scan rate) for **$Na_5AlW_{12}O_{40}$-**, **1-** and **2-**CC electrodes and and the b values are observed to be 0.93, 0.92, and 0.90, respectively. The larger b value of these electrodes indicated the kinetics behaviors are mainly quite attributed to the surface layer capacitance due to the redox reaction of $\{AlW_{12}O_{40}\}$ and the pseudocapacitances from the transformation of W (W^{6+} to W^{5+}).

At the same time, we further studied and separated the contributions of capacitive and diffusion controlled charge from the total charge storage(*Q*), using an approach reported elsewhere[76]:

$$\mathbf{Q=Q_c+Q_d} \qquad (2)$$

The contribution of Q_c is related to the scan rate, mainly due to surface adsorption, which is the combination of a false capacitance and a double-layer capacitor, and the contribution of Q_d is the redox reaction ascribed to the electrode materials. Supposing the semi-infinite linear diffusion processes at a fixed potential, Q_c is obtained by plotting the stored charge(*Q*) vs. the reciprocal of the square root of the scan rate and Q_d vary according to the scan rates. Hence, the total charge stored can be represented by the following equation:

$$\mathbf{Q= Q_c + kv^{1/2}} \qquad (3)$$

Where k is a constant. Fig. S25(a-c) are the linear diagram of *Q* and the square root reciprocal of the scan rate($v^{-1/2}$) for **$Na_5AlW_{12}O_{40}$-**, **1**- and **2**-CC electrodes, shown that the storage charge ability of **2**-CC is the strongest and consistent with the CVs. Q_c and Q_d are estimated and plotted in Fig.S26 and Fig.3(d), demonstrated the normalized contribution ratio of capacitive and diffusion controlled charge storage capacities at 5-100 mV s^{-1}. There are clearly seen that the diffusion-controlled process contribution decreases gradually with increasing the scan rate (from 5 to 100 mV s^{-1}), while the contribution of Q_c increases. Obviously, Q_c is more prominent in these electrode materials and it shows the pseudocapacitive nature of the electrodes.

In our view, **1-** and **2**-CC all show similar CV curves due to their similar structures on the base of same $[AlW_{12}O_{40}]^{5-}$. Since the open metal sites of $\{AlW_{12}\}$ polyanions all are occupied by {-4,4'-bipy-M-4,4 ' -bipy}$_n$ (M= Ag, Cu) polymer chains or small-molecule ethylenediamine ligands. H^+ ions of electrolytes can continuously attack polyoxoanion, and its auxiliary redox process at the open metal center is suitable. Under this experimental condition, $\{AlW_{12}\}$ clusters may provide an effective electron transfer with inner-

View Article Online
DOI: 10.1039/C9TA14103K

cluster. The reversible processes with inner-cluster may better explain the above redox reactions. These redox reactions do not require the dissociation of metal ions from {AlW_{12}} electrode materials, which will effectively preserve the {AlW_{12}} structure effectively in the electrochemical process.

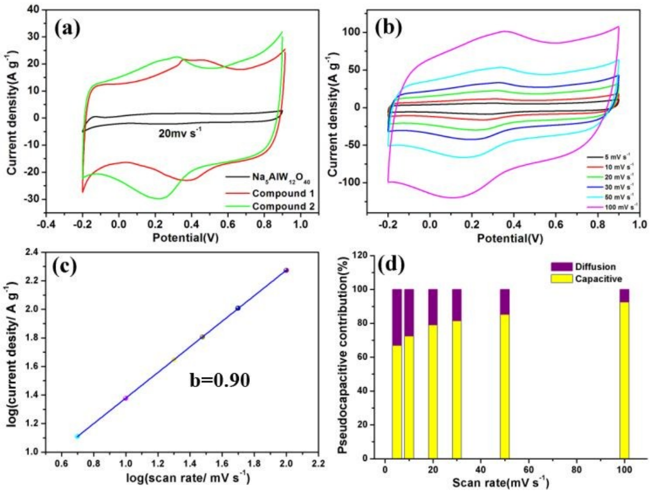

Fig.3 (a) The CVs at the 20 mV s^{-1} scan rate for the different compounds (b) The CVs of **2**-CC at the different scan rates (c) The b value of **2**-CC (d) Q_c and Q_d are estimated for **2**-CC

Galvanostatic charge/discharge

The capacitance performance of these compounds electrodes were studied using the galvanostatic charge-discharge curves (GCD) in 0.5M H_2SO_4 solution with a potential window from -0.2 to 0.9 V. At the current density of 1 A g^{-1}, the specific capacitances of $\mathbf{Na_5AlW_{12}O_{40^-}}$, **1-** and **2**-CC electrodes(Fig.4a) are 130.27F g^{-1}, 478.41F g^{-1} and 625.99F g^{-1}(according to equation (S1)), respectively, which are consistent with the results of CV curves. Fig. S27 and Fig.4b show the GCD curves of **1**-CC and **2**-CC at 1, 2 , 3 , 5 and 10 A g^{-1}. When the current density of 10 A g^{-1}, the specific capacitances (Fig.S28) of two compounds are 85.53 F g^{-1} (**1**-CC) and 115 F g^{-1} (**2**-CC) respectively, demonstrating two compounds have the good rate capability. Meanwhile, the cyclic stability tests of these compounds were carried out at the current density of 10 A g^{-1}, showed that the initial specific volume of **1-** and **2**-CC remained 95.71%(Fig. S29), and 97.62% (Fig. 4c) after 5000 cycles, which are better stability and cycle life of POMs as electrode materials(Table S4).

The electrochemical performances of these compounds were compared by electrochemical impedance spectroscopy (EIS). All the electrodes were produced in the same way and EIS were tested before and after 5000 cycles. Each Nyquist plot consists of a depressed semicircle and a sloping line. The depressed semicircle and the sloping line can belong to the charge transfer process and the solid-state diffusion of ions, respectively. So the internal resistance(R) can be calculated by the depressed semicircle at the high frequency. As showed in Fig.S30, R of **2**-CC(2.62Ω) is much smaller than that of **1**-CC(3.38Ω), and the slope of **2**-CC is greater than that of **1**-CC in the low frequency region, indicates that the addition of ethylenediamine reduces R and enhances the ion-diffusion capacity of electrode materials. As showed in Fig.S31 and Fig.4d, the R values of **1**-CC(2.63 Ω) and **2**-CC(3.41 Ω) after 5000 cycles have little change opposed to those before circulation, indicating that the two compounds have excellent stability and conductivity. The equivalent circuit diagram of EIS for 2-CC is showed in Fig.S32. The ion diffusion coefficient (*D*) of these compounds can be calculated according to the linear relationship of Z' and the reciprocal square root of the frequency in the low frequency region[77],

$$D = \frac{R^2T^2}{2A^2n^4F^4C^2\sigma^2} \quad (4)$$

Where R, *T*, *A*, n, F, *C* and σ are the gas constant, absolute temperature, the surface area of the electrode, the number of electrons per molecule in the oxidation process, the Faraday constant, the concentration of ions and the Warburg factor, respectively.

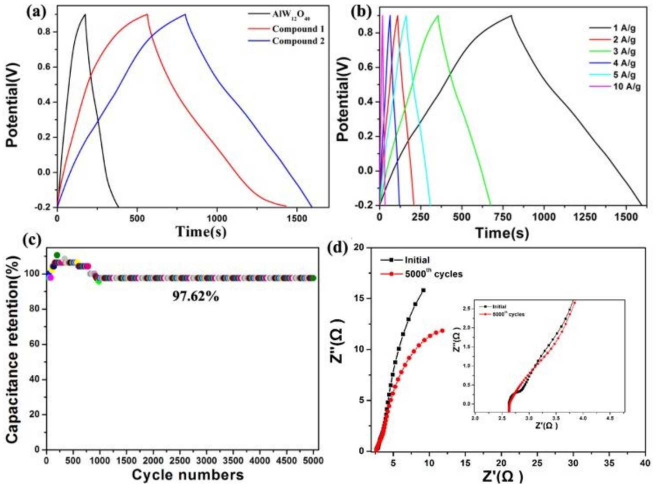

Fig.4 (a) The GCD curves at the 1 A g^{-1} for the different compounds (b) The GCD curves of **2**-CC at the different current densities (c) Cycling stability of **2**-CC after 5000 cycles (d) Impedance analysis of the **2**-CC

In particular, σ is related to *Z*' by the following equation:

$$Z' = B + \sigma\omega^{-1/2} (5)$$

Where B is a constant and *ω* is the frequency. Therefore, *σ* is the slope of the linear relationship between *Z*' and $\omega^{-1/2}$(Fig. S33). The *σ* of **1**-CC and **2**-CC are 19.49, 5.55, respectively, and the d value of **2**-CC is 12 times of **1**-CC. The results show that the small molecule ligands of ethylenediamine and polymer layer can inhibit the charge transfer resistance of the compound and improve the ion transfer ability, which would results in excellent electrochemical performance for these compounds.

We also tested EIS curves for compounds **1-2** in the temperature range 20-80 ℃ (Fig.S34). The electrochemical transfer resistances was obtained from the Nyquist plot by taking the diameter of the semicircle. It suggests that the charge transfer resistance decreases with higher temperature in the range of measured temperature, indicating that the conductivity of compounds **1-2** are strong, which is beneficial to the improvement of capacitance performance. Fig.S35 indicates the Arrhenius plots of above two compounds. The activation energies derived from the plot, which are 39.21kJ·mol^{-1} and 44.86kJ · mol^{-1}, respectively. There are two predominant mechanisms of proton conduction: Grotthuss mechanism[78] and Vehicle mechanism[79]. In the Vehicle mechanism, water assists proton movement by facilitating transport as a H_3O^+ species. It is different to Grotthuss mechanism, in which a large amount of water can assist proton transport through a hydrogen-bonded network. Moreover, the activation energy of the Vehicle mechanism is higher (more than 20.00kJ·mol^{-1}) than that of the Grotthuss mechanism (less than 15.00kJ·mol^{-1}).[80] So, the proton conduction of compounds **1** and **2** occur via Vehicle mechanism. As far as we know, this is the first time to be studied for {AlW_{12}}.

Compared with the performances of other POMs, the higher performance of the **2**-CC can belong to the following reasons(Fig.5): (I) The {AlW_{12}} in the 3D stacking structure is involved in the redox reaction and provides pseudo-capacitance due to the mutual transformation of W^{6+} and W^{5+}(12 electron transfer). (II) On one hand, ethylenediamine ligands can increase the conductivity of compounds and promote electron transfer. On the other hand,the supramolecular interaction of ethylenediamine molecules increased the interaction between the MXene-like layers. (III) The wide layer distance(13.71Å) and the large hole(19.41×15.36Å^2 and 17.90×17.10Å^2) not only promotes the contact area with H^+ ion, but also increase the specific surface area of the compounds. (IV) the covalent bond from the polymers chains inhibit the volume change of AlW_{12} and improve the stability of the structure during charge-discharge process. The polymers chains are rich in channels, which not only act as the pseudocapacitance to facilitate ion diffusion and storage /transport of electrons, but also evenly disperse {AlW_{12}} uniformly and prevent {AlW_{12}} from being dissolved in the electrolyte.

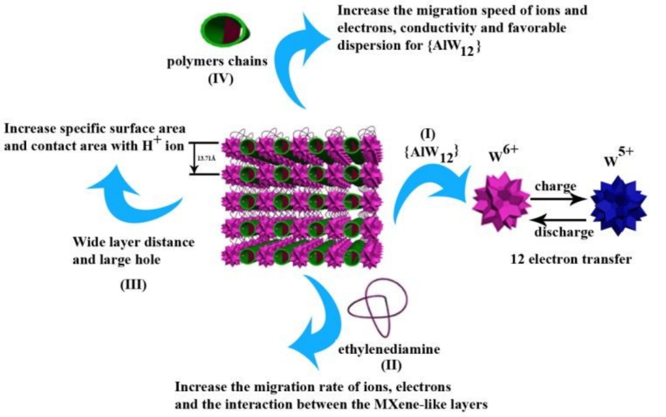

Fig.5 The relationship between the structure and the performance of the super capacitor.

Electrochemical properties of aqueous symmetric supercapacitor device

The symmetrical water system supercapacitor device is assembled with compound **2** as both positive and negative electrodes. Filter paper is used as a separator, and the same two pieces of **2**-CC electrodes (Fig. 6a) with an area of 1×1 cm^2 are parallelly to each other in the 0.5M H_2SO_4. In Fig. S36, the CV curves with 0.1-0.9 V working window at different scan rates, indicated an excellent capacitive behavior and good charge transmission in the electrode even at an extremely high scan rate of 100mV s^{-1}. At the same time, these curves are not strictly linear, which again prove the charge storage mechanism of compound **2** which is the combination of Faraday quasi-capacitance reaction at the anode and cathode. During the charge process, SO_4^{2-} ions migrate to the surface of the electrode and form an electrochemical double layer between the cathode and the electrolyte interface. Meanwhile, H^+ ions diffuse to the anode and inserts into the 3D stacked ion transport system of compound **2**. In the process of discharge, the anodized active material removes H^+ ions and returns H^+ ions back to the electrolyte. In order to further evaluate its electrochemical performance, GCD measurements(Fig. 6b) were performed at 1-10 A g^{-1}. At the current density of 1 A g^{-1}, the supercapacitor shows a high specific capacitance of 71.12 F g^{-1}(according to equation (S2)). With the increase of current densities, the specific capacitance of the device decreases and the retention ratio is considered to be 14.76%(Fig.S37) as the current density increases to 10 A g^{-1}. Energy density(*E*) and power density(*P*) are two crucial factors for practical application of supercapacitors and can be calculated as follows:

$$E= CU^2/2V \quad (6)$$

$$P= E/t \quad (7)$$

Where *C* is the total capacitance of the solid state device, *U* is the operating voltage, *V* is the device volume, *t* is the discharge time. The Ragone plot of the supercapacitor based on the compound **2** is shown in (Fig. 6c). The maximum energy density of 6.32 Wh kg^{-1}can be achieved at a power density of 237 W kg^{-1} from the symmetrical water system supercapacitor device, which is clearly superior to those of many previously reported supercapacitors[81-85]. Moreover, the cycling stability is important considerations for the practical applications of fiexible SCs. Fig. 6d illustrates that the capacitance retention is 92.32% after applying 5000 operational cycles at a current density of 10 A g^{-1}. All the electrochemical studies revealed that compound **2** can be used as the electrode of high stability supercapacitor with increased capacitance and energy density.

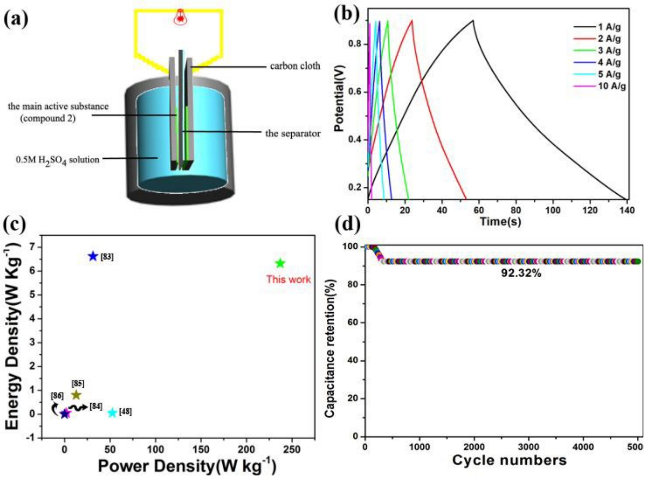

View Article Online
DOI: 10.1039/C9TA14103K

Fig.6 The symmetrical water system SCs device: (a)Working Mechanism of Devices (b) The GCD curves at the different current densities (c)The Ragone plot of the SCs (d) Cycling stability after 5000 cycles

Photocatalytic

With the rapid development of human society, the problem of environmental pollution is becoming ever more serious, especially water pollution endangers human life and health. Photocatalytic degradation of organic pollutants is part of the effective ways to purify water. As the photocatalyst, POMs have the advantages of green, safe, thorough purification and so on. Based on the above considerations, the performances of complexes **1** and **2** against photocatalytic degradation of RhB, MB and MO have been investigated under UV irradiation. During 140min of irradiation, the degradation rate (1-C/C_0) of RhB is 98.21% and 90.83% for compounds **1** and **2** (Fig.S38), and the degradation rate of MB is 91.87% and 90.25% for compounds **1** and **2** (Fig.S39). The degradation rate of MO is 97.38% and 95.43% for compounds **1** and **2** (Fig.S40) after 180min of irradiation, respectively. A contrast experiment was also carried out under the same conditions without any catalyst. Few degradations of RhB, MB and MO were observed in the experiment, as shown in Fig.7.

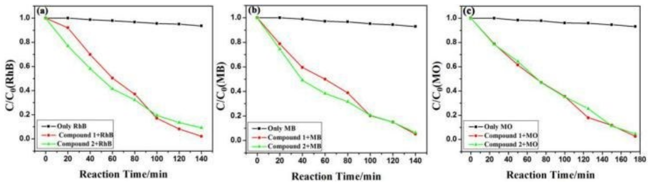

Fig. 7 The photocatalysis decomposition rates of the (a) RhB, (b) MB, (c) MO solution under UV irradiation in the use of the compound **1** and compound **2**.

It can be observed that the degradation process was completed, compounds **1-2** are photocatalysts with high degradation efficiency. Furthermore, the reuse of the catalyst can reduce the cost of the photocatalytic process. The catalyst was centrifuged and filtered and then immersed in another aqueous solution of the same amount of organic dye under the same conditions. As shown in Fig.8, the residual concentration (C/C_0) of the three dyes remained almost unchanged after five catalysts cycles for componds **1-2**. The XRD of compounds **1-2** before and after five cycles photocatalytic reaction are shown in Fig.S11. Comparing the XRD of the two compounds before and after five cycles photocatalytic procedure, the position and intensity of the peaks were nearly identical. These results suggest that compounds **1** and **2** may be a potential photocatalyst in reduction of some organic dyes, which have excellent stability.

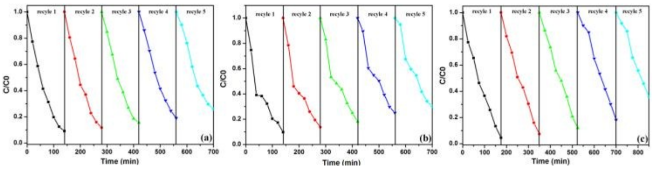

Fig. 8 The photocatalysis decomposition rates of the (a) RhB, (b) MB, (c) MO solution in the use of the compound **1** and compound **2** for 5 recycles.

In order to study the main active components in photocatalytic reaction and the possible mechanism of degradation process, benzoquinone (BQ), EDTA and isopropanol (IPA) as scavengers were added to the photocatalytic system(different dyes) to remove the superoxide radical(•O_2^-), hole (h^+) and hydroxyl radical (•OH). As shown in Fig.9a， it can be seen that the degradation efficiency of MB, MO and RhB by compound **2** decreased slightly after adding BQ and EDTA. However, after the addition of IPA, the degradation efficiency were significantly reduced to 65.35%(MB), 30.42%(MO) and 54.46%(RhB), respectively, suggesting that •OH is the principal active substance in the degradation of three kinds of dyes and the degradation reaction is advanced oxidation processes (AOPs). We take RhB as an example and the possible mechanisms of photocatalysis could be deduced as described below(Fig.9b): during photocatalytic reaction, catalysts {AlW_{12}} form the excited-state species ({AlW_{12}}*) by absorbing light energy higher than the band gap of the {AlW_{12}} (reactions (1)). {AlW_{12}}* captures electrons of H_2O molecules to form •OH (reactions(2)). The reduced {AlW_{12}} is rapidly oxidized by O_2 with the generation of superoxides simultaneously (reactions(3))[86]. These reactions occur circularly when the mixture is radiated in UV light[87-88]. Moreover, the RhB dye is triggered into RhB* molecules in reaction (4). Then, the RhB dye is degraded by the •OH radicals into H_2O and CO_2 after several circular reactions (reaction (5))[89].

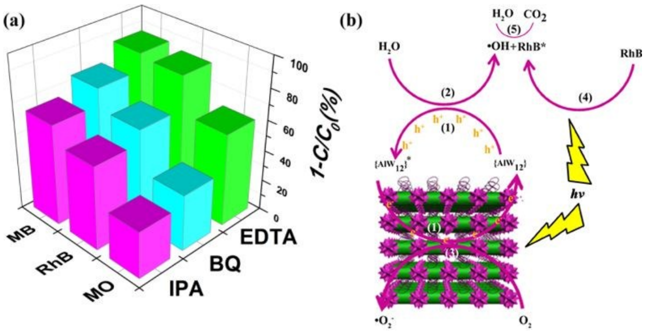

Fig.9 (a) The degradation efficiency of MB, MO and RhB were treated with different scavengers. (b) The possible mechanisms of RhB of photocatalysis for compound **2**

In order to prove that the products of dye degradation are H_2O and CO_2, the samples before and after dye degradation were analyzed by liquid chromatography(LC). As showed in the Fig.S41, there is no peak after degradation, indicating that the final products are mineralized to H_2O and CO_2. In addition, according to the experimental results and related theories[90-93], we propose the possible degradation mechanisms of three kinds of dyes (Fig. 10 and Fig.S42-43). The main results are as follows: Three dyes react with •OH to break the bonds(1-5) to form phenols, aldehydes, quinones, carboxylic acids and alcohols, which are finally mineralized into H_2O and CO_2. (1) the C-S bond between the linked benzene ring and the sulfonic group (2) the azo group (3) the C-N bond of the benzene ring (4) the ring opening cracking of the benzene ring (5) C-C and C-N bond.

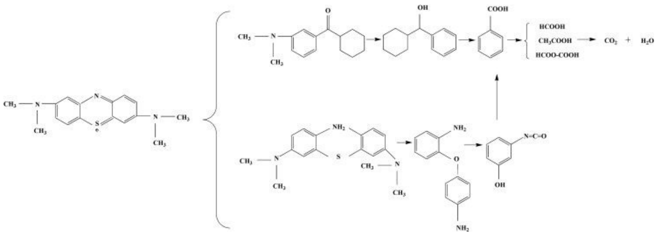

Fig.10 The possible degradation mechanism of MB

It's noteworthy that compounds **1** and **2** have different degradation effects on RhB, MB and MO, which could ascribe to different structures of dyes. Chromophores anilino-, carboxyl and unstable N^+ of RhB are easily damaged by external factors to form some unstable colorless organic intermediates or other isomers of RhB, which causes the solution to fade quickly in photocatalytic process. Anilino- and $=S^+$- of chromophores in MB are destroyed to fade by the external factors. Meanwhile, MB may be removed methyl and decompose smaller organic molecules in UV irradiation. Acid azo structure and alkaline medium of MO are relatively stable, which requires more energy to be removed from methyl and azo reduction in reaction[94]. Nevertheless, RhB and MB need less energy to achieve the structural changes leading to fading of the solution. Besides, the photocatalytic reaction occurs in the adsorbed phase(on the surface of a catalyst), and the model of activation of catalysts is photonic activation by $\{AlW_{12}\}^*$ with light energy higher than the band gap of the $\{AlW_{12}\}$, which leads to intramolecular charge transfer and the formation of an excited-state species ($\{AlW_{12}\}^*$)[95]. It's inferred that identical $\{AlW_{12}\}$ may be the main reason why compounds **1** and **2** exhibit very similar conversions to the same dye. There are several reasons for speculation as follows: $\{AlW_{12}\}$ units possess higher surface charge density, which could adsorb cationic dyes during the reaction process; the second reason may be attributed to the different packing structures of them. The preferential orientations of crystal planes of them should be different, thus the number of POMs on crystal planes perhaps should be different. Furthermore, the introduction of different transition metal complexes and small molecule organic ethylenediamine perhaps has a bearing on the catalytic activity.

Electrochemical sensor

POMs can be redox by multi-step electron transfer without very strict experimental conditions. In addition, the process can not only react quickly and one step at a time, but also do not decompose in the process. Meanwhile, POMs can be used as a good sensor material due to its excellent electrochemical and electrocatalytic performance, and may set off a research upsurge in the field of sensors. Hydrogen peroxide (H_2O_2) is a very important small molecular substance, and its content is closely related to human health and quality of life. Therefore, it is the focus of research in the world to detect hydrogen peroxide conveniently at any time. The electrochemical behaviors of **1-2**-GCEs have been investigated in a 0.1M H_2SO_4 + 0.5M Na_2SO_4 aqueous solution at different scan rates in the potential range from -0.8 to 0.5 V(Fig. S44). In the cyclic voltammetric (CV) curves of **1** and **2**(Fig.S45), there are three reversible redox peaks, which are attributed to three continuous tungsten redox processes, observed that there are an additional irreversible anodic peak (IV) for **1** and for **2**, which should be ascribe to the oxidation of Ag(I) and Cu(I), respectively[96]. Moreover, it is different from the CV curve of supercapacitor because of its electrolyte and voltage window. As Fig.11a and Fig.S46 shown, cyclic voltammograms for the electrocatalytic reduction of H_2O_2 by **1**-GCE and **2**-GCE in 0.1M H_2SO_4 + 0.5M Na_2SO_4 aqueous solution. It can be seen that, with the addition of H_2O_2, the first redox peak remains almost unchanged, nevertheless other reduction peak currents gradually increase, which indicates that the reduction of H_2O_2 is mediated by the reduced species of polyanions in compounds **1** and **2**. According to the equation (8):

$$\mathbf{CAT = 100\% \ \times[Ip\{AlW_{12}\}H_2O_2\text{-}Ip\{AlW_{12}\}]/Ip\{AlW_{12}\}}$$

where $Ip\{AlW_{12}\}H_2O_2$ and $Ip\{AlW_{12}\}$ represent the oxidation peak current of **1**-GCE (or **2**-GCE) with or without H_2O_2, respectively. **1**-GCE and **2**-GCE have the catalytic efficiency of 96.69% and 165.65% for 40 mM H_2O_2. Depending on the above investigations, we can get some information about the **1**-GCE and **2**-GCE for their potential application in the electrochemistry and electrocatalysis fields. From the above measurement results, it can be seen that **1**-GCE and **2**-GCE have good electrocatalytic activity for the oxidation of H_2O_2, and there are possible to become H_2O_2 sensor materials. Therefore, we will test a series of sensing performance of **1**-GCE and **2**-GCE to verify whether they can become H_2O_2 sensor materials in practical applications. In electrochemical sensors, sensitivity and selectivity depend on the choice of application potential, so we detected seven kinds of interfering substances ($CaCl_2$, $MgSO_4$, NaCl, glucoes, $ZnSO_4$, KIO_3 and $NaNO_2$) at different application potentials. As shown in the Fig.S47 and Fig.11b, as the applied potential moves forward, the catalytic current for H_2O_2 also increases gradually. These results show that the more sensitive the applied potential is shifted in the forward direction, and the response current is maximum at -0.5V. For **1**-GCE, the current responses of $MgSO_4$ are 2.40%(-0.6V), 3.87%(-0.7V) and 16.06%(-0.8V) of H_2O_2 at the different potentials, and the current responses of $CaCl_2$ are 4.61%(-0.6V) 13.32%(-0.7V) and 7.89%(-0.8V) of H_2O_2 at the different potentials. The other five substances have little current response in the range of-0.4--0.8V. For compound **2**, the current responses of $CaCl_2$ are 4.70% (- 0.4V)and 4.13%(-0.6V) of H_2O_2, and the current response of $NaNO_2$ is 3.58%(-0.4V) of H_2O_2. The other substances have little current response at different voltages of -0.4--0.8V. These above data show that **1**-GCE and **2**-GCE electrochemical sensors have excellent selectivity and anti-interference ability, and -0.5 V is chosen as the best application potential to detect H_2O_2.

The sensitivity and detection range of the sensor are two important evaluation indexes for the sensor materials. Therefore, we use amperometric current-time (i-t) measurements to study the senor

View Article Online
DOI: 10.1039/C9TA14102H

performance of **1**-GCE and **2**-GCE. As shown in Fig. S48 and Fig. 11c, the measurements are performed by adding different concentrations of H_2O_2 in 0.1M H_2SO_4 + 0.5M Na_2SO_4 aqueous solution at the potential of -0.5V. With the addition of H_2O_2, the response current of **1**-GCE and **2**-GCE are gradually enhanced. However, the response current of **2**-GCE is more than **1**-GCE, indicating that the addition of ethylenediamine molecule is beneficial to enhance the catalytic performance of H_2O_2, which is consistent with the conclusion obtained by CVs. A calibration curve(Fig. S49 and Fig. 11d) is drawn to reflect the relationship between the response current(I) and the different concentrations of H_2O_2(C): I= -0.073185C-39.71112 R^2=0.971(**1**-GCE), I= -0.07052C-98.9396 R^2=0.993(**2**-GCE). The broad detection range of the sensors to H_2O_2 are 1.20 mM to 3.20mM (**1**-GCE) and 19.95 μM to 0.90 mM (**2**-GCE)(signal-to-noise ratio:S/N=3) with the detection limit of 0.93μM, 0.86μM and the response time is 4s, 2s, respectively. In order to reflect the properties of compounds **1** and **2** sensor materials more intuitively, we compare their properties with some reported studies in Table S5, shown that the two sensors have a wider linear range and a lower detection limit. These properties are due to the rapid and progressive electronic transfer performance and excellent catalytic properties between {AlW_{12}}, the polymer chains(Cu or Ag) can accelerate the transfer rate between electrons, while the small ethylenediamine molecule provides more active sites.

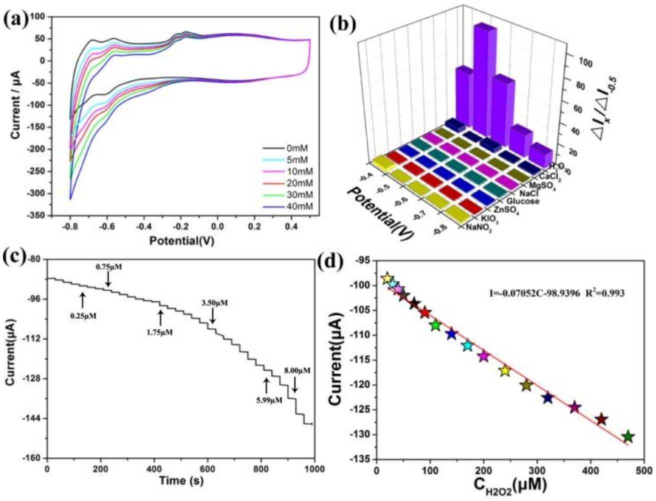

Fig. 11 (a) Reduction of H_2O_2 at **2**-GCE (Scan rate: $50mVs^{-1}$) (b)The selectivity profile of compound **2** at -0.4~-0.8V (c)The i-t curve of compound **2** with successive additions of H_2O_2 (d)The linear relationship between the current response of compound **2** and the concentration of H_2O_2

The stability and repeatability are important in practice of the excellent electrochemical sensors. The stability of **1**-GCE and **2**-GCE are the CVs of 1000 cycles at a 50 m V s^{-1} with -0.8-0.5 V in the 0.1M H_2SO_4 + 0.5M Na_2SO_4. As shown in Fig.S50, the peak current and peak potential did not change significantly after 1000 cycles, and the retention rates were 83.89%(**1**-GCE) and 93.32% (**2**-GCE), indicating that compounds **1** and **2** had good stability after continuous cyclic voltammetry scanning. The reproducibility of **1**-GCE and **2**-GCE are carried out by immersing ten identical electrodes under the same condition in the above-described analyte solution. As shown in Fig.S51, standard deviation(RSD) of **1**-GCE and **2**-GCE are 2.27% and 2.04%, show that the sensors have excellent reproducibility.

The mechanism of the sensor is explained according to the previous literature[97-98], and the equation is as follows:

$$H_2O_2 + e^- \rightarrow OH_{ad} + OH^- \quad (a)$$

$$OH_{ad} + e^- \rightarrow OH^- \quad (b)$$

$$2OH^- + 2H^+ \rightarrow 2H_2O \quad (c)$$

During the reaction, the key step of controlling the reaction rate is the formation of OH_{ad}. However, compound **2** has better sensor performance than compound 1 and other studies are as following reasons: (1) On the one hand, polymer chains and ethylenediamine ligands are beneficial to the uniform dispersion of {AlW_{12}} and promote electron transfer. On the other hand, the covalent bond of the polymer chains and the supramolecular interaction of ethylenediamine molecules inhibit the volume change of {AlW_{12}} and improve the stability and optimal contact property of the material. (2) The {AlW_{12}} in the stacking 3D structure is involved in the redox reaction and provides electrons due to the mutual transformation of W^{6+} and W^{5+}, which is beneficial to the forward movement of the reaction. (3) Polymers chains are rich in channels, which not only promote the diffusion and storage/transmission of electrons, but also evenly disperse {AlW_{12}} uniformly to prevent {AlW_{12}} from being dissolved in the electrolyte. (4) π-π binding between different conductive polymer chains not only promotes the polymerization of polymer chains on the surface of {AlW_{12}}, but also shortens the diffusion time, improves the efficiency of proton transfer and the reaction kinetics on the surface of electrode material. Therefore, the research of compounds **1-2** provides a new idea for novel sensor materials.

Experimental

Synthesis of compound **1**: A mixture of $Na_2WO_4 \cdot 2H_2O$ (0.33 g, 1mmol), $Al(NO_3)_3 \cdot 9H_2O$(0.038 g, 0.1mmol), $AgNO_3$ (0.05 g, 0.3mmol), 4,4'-bipy(0.028 g, 0.2mmol), and H_2O (10mL) was stirred for half an hour in air. Then the pH was adjusted to 4.0 by diluting ethylenediamine solution and 4 M HNO_3. The mixture was then transferred to a Teflon-lined autoclave (23mL) and kept at 160 ℃ for 4 days. After the sample was slowly cooled to room temperature, the light yellow crystals were filtered off, washed with distilled water, and dried in a desiccator at room temperature to give a yield of 58.6% based on W. Anal. Calc. for C30H24Ag3AlN6O44W12: C, 9.65; H, 0.64; Ag, 8.68; N, 2.25; Al, 0.72; W, 59.18(%). Found: C, 9.41; H, 0.71; Ag, 8.63; N, 2.31; Al, 0.71; W, 59(%). Selected IR (KBr pellet, cm^{-1}): 3496(m), 1608(s), 953(s), 887(s), 802(m), 766(s).

View Article Online
DOI: 10.1039/C9TA14103K

Synthesis of compound **2**: The synthesis of compound **2** is the same as that of compound **1** except $AgNO_3$ were replaced by $CuCl_2 \cdot 6H_2O$ (0.05g, 0.3mmol), the orange crystals were filtered off, washed with distilled water, and dried in a desiccator at room temperature to give a yield of 55.2% based on W. Anal. Calc.C30H24Cu3AlN6 O41W12 for: C, 10.14; H, 0.68; Cu,5.41; N, 2.37; Al, 0.76; W, 62.18(%). Found: C, 10.24; H, 0.64; Cu, 5.35; N, 2.34; Al, 0.73; W, 62.24(%). Selected IR (KBr pellet, cm^{-1}): 3442(m), 1612(s), 962(s), 882(s), 812(m), 761(s).

Conclusions

In summary, using $\{AlW_{12}\}$ polyoxianions, metal ions, 4,4-bipy and ethylenediamine as raw materials, two kinds of MXene-like single crystals were successfully synthesized and directly used as supercapacitors, sensor electrode materials and photocatalysts. The capacitors of **1**-CC and **2**-CC electrodes are 478.41 and 625.99 F g^{-1} (at 1.0 A g^{-1}), and the cyclic stability of two electrodes are above 95% retention after 5000 cycles. A fully symmetrical water system supercapacitor was prepared with compound **2**, and the maximum energy density of 6.32 Wh kg^{-1} can be achieved at a power density of 237 W kg^{-1}, which is clearly superior to those of many previously reported supercapacitors. Meanwhile, compounds **1**-**2** were used as electrode materials to test the new sensitive current hydrogen peroxide sensor, display that the linear ranges are 1.20 mM to 3.20mM (**1**-GCE) and 19.95 µM to 0.90 mM (**2**-GCE)with the detection limit of 0.93µM, 0.86µM (response time: 4s, 2s). In addition, compounds exhibits excellent photocatalytic degradation ability for typical dyes.•OH is the principal active substance and the degradation reaction is AOPs. Three dyes react with •OH to break the bonds to form phenols, aldehydes, quinones, carboxylic acids and alcohols, which are finally mineralized into H_2O and CO_2.

Conflicts of interest

There are no conficts of interest to declare.

Acknowledgements

This work was supported the National Natural Science Foundation of China (Grants 21571044 and 21771046 to B.Z.) and the Natural Science Foundation of Heilongjiang Province (Grants JJ2016JQ0037 and B2017007 to B.Z.)

Notes and references

1 L. Wang, X. Xie, K. N. Dinh, Q. Y. Yan, J. M. Ma, *Coord. Chem. Rev.*, 2019, **397**, 138-167. DOI: org/10.1016/j.ccr.2019.06.015

2 Y. R. Qi, Y. X. Lu, F. X. Ding, Q. Q. Zhang, H. Li, X. J. Huang, L. Q. Chen, Y. S. Hu, *Angew. Chem. Int. Ed.*, 2019, **58**, 4361-4365. DOI: 10.1002/anie.201900005

3 L. Croguennec, M R Palacin, *J. Am. Chem. Soc.*, 2015, **137**, 3140-3156. DOI:10.1021/ja507828x

4 X. Y. Yu, L. Yu , X. W. Lou, *Adv. Energy Mater.*, 2016, **6**, 1501333-1501346. DOI:10.1002/aenm.201501333

5 Z. Y. Wang, L. Zhou, X. W. Lou, *Adv. Mater.*, 2012, **24**, 1903-1911. DOI:10.1002/adma.201200469

6 H. Huang, S. Gao, A. m. Wu, K. Cheng, X. n. Li, X. x. Gao, J. j. Zhao, X. L. Dong, G. Z. Cao, *Nano Energy*, 2017, **31**, 74-83. DOI:10.1016/j.nanoen.2016.10.059

7 S. L. Zhai, H. E. Karahan, C. J. Wang, Z. X. Pei, L. Wei, and Y. Chen, *Adv. Mater.*, 2019, 1902387. DOI: 10.1002/adma.201902387

8 L. B. Wang, H. L. Yang, X. X. Liu, R. Zeng, M. Li, Y. H. Huang, X. L. Hu, *Angew. Chem. Int. Ed.*, 2018, **56**, 1105-1110. DOI: 10.1002/anie.201609527

9 Y. Z. Zhang, Y. Wang, T.Cheng, L. Q. Yao, X. C. Li, W. Y. Lai and W. Huang, *Chem. Soc. Rev.*, 2019, **48**, 3229-3264. DOI: 10.1039/c7cs00819h

10 R. R. Salunkhe, Y. H. Lee, K. H. Chang, J. M. Li, P. Simon, J.Tang, N. L. Torad, C. C. Hu, and Y. Yamauchi, *Chem. Eur. J.*, 2014, **20**, 1-16. DOI: 10.1002/chem.201403649

11 H. Chen, S. Zhou, L. Wu, *ACS Appl. Mater. Interfaces*, 2014, **6**, 8621-8630. DOI:10.1021/am5014375

12 R. R. Salunkhe, S. H. Hsu, K. C. W. Wu, Y. Yamauch, *ChemSusChem*, 2014, **7**, 1551-1556. DOI: 10.1002/cssc.201400147

13 Q. Zhang, A. A Zhou, J. J. Wang , J. F. Wu, H. Bai, *Energy Environ. Sci.*, 2017, **10**, 2372-2382. DOI:10.1039/C7EE02018J

14 A. Borenstein, O. Hanna, R. Attias, S. Luski, T. Brousse and D. Aurbach, *J. Mater. Chem. A*, 2017, **5**, 12653-12672. DOI:10.1039/C7TA00863E

15 A. González, E. Goikolea, J. A. Barrena, R. Mysyk, *Renew Sust Energ Rev.*, 2016, **58**, 1189-1206. DOI: 10.1016/j.rser.2015.12.249

16 F. Yu, L. Wang, Y. Wang, X. J. Shen, Y. J. Cheng and J. Ma, *J. Mater. Chem. A*, 2019, **7**, 15999-16027. DOI:10.1039/c9ta01264h

17 M.Volokh, G. Peng, B. Jesús, *Angew. Chem. Int. Ed.*, 2019, **58**, 6138-6151. DOI:10.1002/anie.201806514

18 V. Piradi, X. P. Xu, Z. Y. Wang, J. Ali, Q. Peng, F. Liu, X. J. Zhu, *ACS Appl. Mater. Interfaces*, 2019, **11**, 6283-6291. DOI:10.1021/acsami.8b19240

19 L. L. Ye, Y. P. Xie, Y. Q. Xiao, J. L. Song, C. Li, H. T. Fu, K. K. Weng, X. H. Lu, S. T. Tan and Y. M. Sun, *J. Mater. Chem. A*, 2019, **7**, 8055-8060. DOI: 10.1039/C9TA01285K

20 M. Marandi, P. Talebi, S. Bayat, *J Mater Sci-Mater. El.*, 2019, **30**, 3820-3832. DOI:10.1007/s10854-019-00666-w

21 Q. F. Meng, K. F. Cai, Y. X. Chen, L. D. Chen, *Nano Energy*, 2017, 36, 268-285. DOI: 10.1016/j.nanoen.2017.04.040

22 Y. X. Chen, W. J. Ma, K. F. Cai, X. W. Yang, C. J. Huang, *Electrochim. Acta*, 2017, **246**, 615-624. DOI:10.1016/j.electacta.2017.06.102

23 A. Dolbecq, E. Dumas, C. R. Mayer and P. Mialane, *Chem Rev.*, 2010, **110**, 6009-6048. DOI:10.1021/cr1000578

24 S. T. Zheng, J. Zhang, X. X. Li, W. H. Fang and G. Y. Yang, *J. Am. Chem. Soc.*, 2010, **132**, 15102-15103. DOI:10.1021/ja105986b

25 A. K. C. Gallegos, M. L. Cantu, N. C. Pastor and P. G. Romero, *Adv. Funct. Mater.*, 2005, **15**, 1125-1133. DOI:10.1002/adfm.200400326

26 H. N. Miras, J. Yan, D. L. Long and L. Cronin, *Chem. Soc. Rev.*, 2012,**41**, 7403-7430. DOI:10.1039/C2CS35190K

27 T. Ueda, *Chemelectrochem*, 2018, **5**, 823-838. DOI:10.1002/celc.201701170

28 Y. C. Ji, L. J. Huang, J. Hu, C. Streb and Y. F. Song, *Energy Environ. Sci.*, 2015, **8**, 776-789. DOI:10.1039/C4EE03749A

29 U. Kortz, A. Müller, J.V Slageren, J. Schnack, N. S. Dalal, M. Dressel, *Coord. Chem. Rev.*, 2009, **253**, 2315-2327. DOI:org/10.1016/j.ccr.2009.01.014

30 Y. W. Liu, S. M. Liu, D. F. He, N. Li, Y. J. Ji, Z. P. Zheng, F. Luo, S. X. Liu, Z. Shi, and C.W. Hu, *J. Am. Chem. Soc.*, 2015, **137**,12697-12703. DOI:10.1021/jacs.5b08273

View Article Online
DOI: 10.1039/C9TA14105K

31 S. S. Wang, G. Y. Yang, *Chem. Rev.*, 2015, **115**, 4893-4962. DOI:10.1021/cr500390v

32 Y. Zhang, Y. F. Wang, X. Y. Meng, L. Yu, Y. Ding, M. D. Chen, *J Photoch Photobio A*, 2018, **355**,371-376. DOI:10.1016/j.jphotochem.2017.08.016

33 M. L. Wei, X. X. Wang, J. J. Sun, X. Y. Duan, *J Solid State Chem.*, 2013, **202**, 200-206. DOI:10.1016/j.jssc.2013.03.041

34 L. Wang, B.B. Zhou, K. Yu, Z.H. Su, S. Gao, L.L. Chu, J.R. Liu, and G.Y. Yang, *Inorg. Chem.*, 2013, **52**, 5119-5127.DOI:10.1021/ic400019r

35 Z. Zhou, D. Zhang, L. Yang, P. Ma, Y. Si, U. Kortz, J. Niu, J. Wang, *Chem. Commun.*, 2013, **49**, 5189-5191. DOI: 10.1039/C3CC41628C

36 L. Wang, K. Yu, B.B. Zhou, Z.H. Su, S. Gao, L.L. Chu and J. R. Liu, *Dalton Trans.*, 2014, **43**, 6070-6078. DOI:10.1039/c3dt53030b

37 L. Wang, K. Yu, J. Zhu, B. B. Zhou, J. R. Liu and G. Y. Yang, *Dalton Trans.*, 2017, **46**,2874-2883,DOI: 10.1039/c6dt02420c

38 L. Wang, S.B. Li, K. Yu, J. Zhu, H.J. Shi, B.B. Zhou, and J.R. Liu, *Adv. Healthcare Mater.*, 2019, **8**, 1900471. DOI: 10.1002/adhm.201900471

39 H. X. Zhao, L. Tao, F.M. Zhang, Y. Zhang, Y.Q. Liu, H.J. Xu, G.W. Diao, L.B. Ni, *Chem. Commun.*, 2019, **55**, 1096-1099, DOI: 10.1039/C8CC07884J

40 L. Zhang, L. Ning, Z. F. Zhang, S. B. Li, H. Yan, H. J. Pang, H. Y. Ma, *Sensors Actuat B-Chem*, 2015, **221**, 28-36. DOI:10.1016/j.snb.2015.06.070

41 J. W. Zuo, Z. F Zhang, J. Jiao, H. J. Pang, D. Zhang, H. Y. Ma, *Sensors Actuat B-Chem*, 2016, **236**, 418-424. DOI: 10.1016/j.snb.2016.05.159

42 N. S. Lopa, M. M. Rahman, F. Ahmed, S. Chandra Sutradhar, T. Ryu and W. Kim,*Electrochim. Acta*, 2018, **274**, 49-56. DOI:10.1016/j.electacta.2018.03.148

43 Z. Y. Bai, C. L. Zhou, H. B. Xu, G. N. Wang, H. J. Pang, H. Y. Ma, *Sensors Actuat B-Chem*, 2017, **243**, 361-371. DOI:10.1016/j.snb.2016.11.159

44 L. Zhang, S. B. Li, Z. F. Zhang, L. C. Tan, H. J. Pang, H. Y. Ma, *J Electroanalytical Chem.*, 2017, **807**, 97-103. DOI:10.1016/j.jelechem.2017.11.030

45 D. Zhu, J. W. Zuo, L. C. Tan, H. J. Pang and H. Y. Ma, *New J Chem.*, 2019, **43**, 1053-1062. DOI:10.1039/C8NJ04570D

46 A. Yamada and J. B. Goodenough, *J Electrochem. Soc.*, 1998, **145**, 737-743. DOI: 10.1149/1.1838339

47 Y. G. Wang, X.G. Zhang, *Solid State Ionics*, 2004, **166**, 61-67. DOI: 10.1016/j.ssi.2003.11.001

48 G. N. Wang, T. T. Chen, S. B. Li, H. J. Pang, H. Y. Ma, *Dalton Trans*, 2017, **46**, 13897-13902. DOI:10.1039/C7DT02230A

49 H. J. Pang, J. Chen, J.Peng, J. Q. Sha, Z. Y. Shi, A. X. Tian, P. P. Zhang, *Solid State Sci.* 2009, **11**, 824-828.DOI: 10.1016/j.solidstatesciences.2008.11.008

50 H. Y. Chen, G. Wee, R. A. Oweini, J. Friedl, K. S. Tan,Y. X. Wang, C. L. Wong, U. Kortz, U, Stimming, M. Srinivasan, *ChemPhysChem*.,2014, **15**, 2162-2169. DOI: 10.1002/cphc.201400091

51 H. N. Wang, M. Zhang, A. M. Zhang, F. C. Shen, X. K. Wang, S. N. Sun, Y. J. Chen, and Y. Q. Lan, *ACS Appl. Mater. Interfaces*, 2018, **10**, 32265-32270. DOI: 10.1021/acsami.8b12194

52 K. B. Wang, Z. K. Wang, S. Wang, Y. Chu, R. Xia, X. Y. Zhang, H. Wu, *Chem. Eng. J.*, 2019, **367**, 239-248. DOI:10.1016/j.cej.2019.02.145

53 K. P. Wang, K. Yu, J. H. Lv, M. L. Zhang, F. X. Meng, and B. B. Zhou, *Inorg. Chem.*, 2019, **58**, 7947-7957. DOI: 10.1021/acs.inorgchem.9b00692

54 N. N. Du, L. G. Gong, L. Y. Fan, K. Yu, H. Luo, S. J. Pang, J. Q. Gao, Z. W. Zheng, J. H. Lv, and B. B. Zhou, *ACS Appl. Nano Mater.*, 2019, **2**, 3039-3049. DOI:10.1021/acsanm.9b00409

55 Y. Chen, B. B. Zhou, J. X. Zhao, Y. G. Li, Z. H. Su, Z. F. Zhao, *Inorg. Chim. Acta*, 2010, **363**, 3897-3903. DOI:10.1016/j.ica.2010.07.060

56 M. M. Heravi, M. Mirzaei, S. Y. S. Beheshtiha, V. Zadsirjan, F. M. Ameli, *Appl Organometal Chem.*, 2018, **32**, e4479. DOI:10.1002/aoc.4479

57 S. Matsunaga, Y. Inoue, T. Otaki, H. Osada, and K. Nomiya, *Z. Anorg. Allg. Chem.*, 2016, **642**, 539-545. DOI: 10.1002/zaac.201500794

58 C. N. Kato, T. Kashiwagi, W. Unno, M. Nakagawa and H. Uno, *Inorg Chem.*, 2014, **53**, 4824-4832. DOI:10.1002/chin.201430020

59 C. N. Kato, Y. Makino, W. Unno and H. Uno, *Dalton Trans.*, 2013, **42**, 1129-1135. DOI:10.1039/C2DT32107F

60 Q. Lan, Y. Lu, Y. G. Li, H. Q. Tan, D. Liu, E. B. Wang, *Transition Met. Chem.*, 2012, **37**, 445-451. DOI:10.1007/s11243-012-9608-1

61 Y. Q. Huang, Train. Res. J.Hubei Univ.Edu., 2004, **21**, 20-21.

62 H. I. S. Nogueira, F. A. AlmeidaPaz, P. A. F. Teixeira, and J. Klinowski, *Chem. Commun.*, 2006, **28**, 2953-2955, DOI:10.1039/b605973b

63 S. R. Bajpe, S. Henke, J.H. Lee, P. D. Bristowea and A. K. Cheetham, *CrystEngComm*, 2016, **18**, 5327-5332. DOI: 10.1039/c5ce02088c

64 Y.W. Li, L.Y. Guo, H.F. Su, M. Jagodič, M. Luo, X.Q. Zhou, S.Y. Zeng, C.H. Tung, D. Sun, and L.S. Zheng, *Inorg. Chem.*, 2017, **56**, 52481-2489. DOI:10.1021/acs.inorgchem.6b02601

65 S.B. Li, L. Zhang,Y.Q. Lan, K. P. O’Halloran,H.Y. Ma and H.J. Pang, *Chem. Commun.*, 2018, **54**, 1964-1967. DOI: 10.1039/c7cc09223g

66 M. T. Li,X. Y. Yang, J. S. Li, N. Sheng, G. D. Liu, J. Q. Sha, and Y. Q. Lan, *Inorg. Chem.*, 2018, **57**, 3865-3872. DOI:10.1021/acs.inorgchem.7b03228

67 X. Li, X. Y. Yang, J. Q. Sha, T. Han, C. J. Du, Y. J. Sun, and Y. Q. Lan, *ACS Appl. Mater. Interfaces*, 2019, **11**, 16896-16904. DOI:10.1021/acsami.9b00872

68 Y. Hou, D. F. Chai, B. N. Li, H. J Pang, H. Y Ma, X. M. Wang and L. C. Tan, *ACS Appl. Mater. Interfaces*, 2019, **11**, 20845-20853. DOI:10.1021/acsa mi.9b04649

69 D. Chai, C. J. Gómez-García, B. Li, H. Pang, H. Ma, X. Wang, L. Tan, *Chem. Eng. J.*, 2019, **373**, 587-597. DOI: 10.1016/j.cej.2019.05.084

70 M. Naguib, J. Come , B. Dyatkin, V. Presser, P. L. Taberna, P. Simon, M. W. Barsoum, Y. Gogotsi, *Electrochem Commun.*, 2012, **16**, 61-64. DOI:10.1016/j.elecom.2012.01.002

71 X. Zhang, Z. H. Zhang, Z. Zhou, *J Energy Chem.*, 2018, **27**, 73-85. DOI:10.1016/j.jechem.2017.08.004

72 W. Liu, H. H. Thorp, *Inorg. Chem.*, 1993, **32**, 4102-4105. DOI:10.1021/ic00035a012

73 C. Rocchiccioli-Deltcheff, M. Fournier, R. Franck, and R. Thouvenot, *Inorg. Chem.*, 1983, **22**, 207-216. DOI: 0020-1669/83/1322-0207

74 H. Zhang, K. Yu, S. Gao, C. M. Wang, C. X Wang, H. Y. Wang and B. B. Zhou, *CrystEngComm.*, 2014, **16**, 8449-8456. DOI:10.1039/C4CE01029A

75 D. P. Dubal, N. R. Chodankar, A. Vinu, D. H. Kim, P. Gomez-Romero, *Chemsuschem*, 2017, **10**, 2742-2750. DOI: 10.1002/cssc.201700792

76 N. R. Chodankar, D. P. Dubal, Y. Kwon, D. H. Kim, *NPG Asia Mater.*, 2017, **9**, e419. DOI:10.1038/am.2017.145

77 S. G. Mohamed, I. Hussain, J. J. Shim, *Nanoscale*, 2018, **10**, 6620-6628. DOI:10.1039/C 7NR07338K

78 N. Agmon, The Grotthuss Mechanism, *Chem Phys Lett.*, 1995, **244**, 456-462. DOI:10.1016/0009-2614(95)00905-J

79 K. D. Kreuer, W. Weppner, A. Rabenau. *Angew. Chem. Int. Ed.*, 1982, **21**, 9-208. DOI:10.1002/anie.198202082

80 K. Cheückiewicz, G. Zúukowska, W. Wieczorek, *Chem. Mater.*, 2001, **13**, 379-384. DOI:10.1021/cm0011155

View Article Online
DOI: 10.1039/C9TA14103K

81 P. G. Romero, M. Chojak,K. C. Gallegos, J. A. Asensio, P. J. Kulesza, N. C. Pastor, M. L. Cantú, *Electrochem. Commun.*, 2003, **5**, 149-153. DOI:10.1016/s1388-2481(03)00010-9

82 Z. L. Guo, L. Yang, W. Wang, L. X. Cao and B. H. Dong, *J. Mater. Chem. A*, 2018, **6**, 14681-14688. DOI:10.1039/C8TA03812K

83 D.Y. Fu, H. W. Li, X. M. Zhang, G. Y. Han, H. H. Zhou, Y. Z. Chang, *Mater. Chem. Phys.*, 2016, **179**, 166-173. DOI: 10.1016/j.matchemphys.2016.05.024

84 K. Qi, R. Z. Hou, S. Zaman, Y. B.Qiu, B.Y. Xia, and H. W. Duan, *ACS Appl. Mater. Inter*, 2018, **10**, 18021-18028. DOI:10.1021/acsami.8b05802

85 L. Wang, X. Feng, L. T. Ren, Q. H. Piao, J. Q. Zhong, Y. B. Wang, H. W. Li, Y. F. Chen, and B. Wang, *J. Am. Chem. Soc.*, 2015,**137**, 4920-4923.DOI:10.1021/jacs.5b01613

86 L. Li, J. W. Sun, J. Q. Sha, G. M. Li, P. F. Yan and C. Wang, *CrystEngComm.*, 2015, **17**, 633-641. DOI:10.1039/C4CE01725K

87 L.S. Cavalcante, J.C. Sczancoski, N.C. Batista, E. Longo, J.A. Varela, M.O. Orlandi, *Adv Powder Tech.*, 2013, **24**, 344-353. DOI: 10.1016/j.apt.2012.08.007

88 L. S. Cavalcante, F. M. C. Batista, M. A. P. Almeida, A. C. Rabelo, I. C. Nogueira, N. C. Batista, J. A. Varela, M. R. M. C. Santos, E. Longo and M.S. Li, *RSC Adv.*, 2012, **2**, 6438-6454. DOI: 10.1039/c2ra20266b

89 Y. Q. Jiao, C.Qin, H.Y. Zang, W.C. Chen, C.G, Wang, T. T. Zheng, K. Z. Shao and Z. M. Su, *CrystEngComm*, 2015, **17**, 2176-2189. DOI:10.1039/C4CE02007C

90 T. S. Natarajan, M. Thomas, K. Natarajan, H. C. Bajaj, R. J. Tayade, *Chem. Eng. J.*, 2011, **169**, 126-134. DOI:10.1016/j.cej.2011.02.066

91 A. Houas, H. Lachheb, M. Ksibi, E. Elaloui, C. Guillard, J. M. Herrmann, *Appl Catal B: Envir.*, 2011, **31**, 145-157. DOI:10.1016/S0926-3373(00)00276-9

92 J. J. Ma, L. C. Zhou, W. F. Dan, H. Zhang, Y. M. Shao, C. Bao, L. Y. Jing, *J Colloid and Inter Sci.*, 2015, **446**, 298-306. DOI: 10.1016/j.jcis.2015.01.036

93 L. Gomathi Devi, S. Girish Kumar, K. Mohan Reddy, C. Munikrishnappa, *J Hazardous Mater.*, 2009, **164**, 459-467. DOI:10.1016/j.jhazmat.2008.08.017

94 R. B. Huang, S. Li, J. S. Hu, G.W. Qin, *J. Mater. Metallurgy.*, 2012, **11**, 303-307. DOI: 10.14186/j.cnki.1671-6620.2012.04.015

95 H. Fu, Y. G. Li, Y. Lu, W. L. Chen, Q. Wu, J. X. Meng, X. L. Wang, Z. M. Zhang and E. B. Wang, *Cryst. Growth Des.*, 2011, **11**, 458-465. DOI:10.1021/cg101224r

96 J. Q. Sha, J. Peng, Y. Q. Lan, Z. M. Su, H. J. Pang, A. X. Tian, P. P. Zhang, and M. Zhu, *Inorg. Chem.*, 2008, **47**, 5145-5153. DOI:10.1021/ic702407y

97 F. H. Meng, X. L. Yan, J. G. Liu, J. Gu, Z. G. Zou, *Electrochim. Acta*, 2011, **56**, 4657-4662. DOI: 10.1016/j.electacta.2011.02.105

98 B. Li, H. Y. Song, Z. P. Deng, L. H. Huo, S. Gao,*Sensors Actuat B-Chem*, 2019, **288**, 641-648. DOI: 10.1016/j.snb.2019.03.054

View Article Online
DOI: 10.1039/C9TA14103K

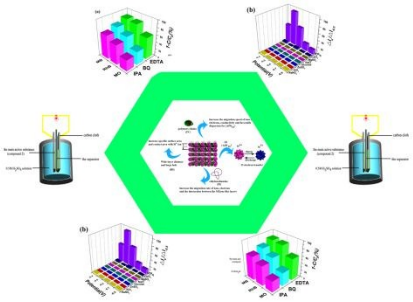

The covalent conductive polymer chain and organic ligand ethylenediamine modified MXene-like-{$AlW_{12}O_{40}$} compounds are proposed to discover promising photo-electrically active materials